AGU PUBLICATIONS

JGR

Journal of Geophysical Research: Atmospheres

RESEARCH ARTICLE
10.1002/2017JD027362

The Complex Refractive Index of Volcanic Ash Aerosol Retrieved From Spectral Mass Extinction

Benjamin E. Reed[1], **Daniel M. Peters**[1,2], **Robert McPheat**[2], **and R. G. Grainger**[3]

[1] Atmospheric, Oceanic and Planetary Physics, University of Oxford, Oxford, UK, [2] RAL Space, STFC Rutherford Appleton Laboratory, Harwell, UK, [3] COMET, Atmospheric, Oceanic and Planetary Physics, University of Oxford, Oxford, UK

Key Points:
- The complex refractive indices of eight samples of volcanic ash aerosol were retrieved from measurements of spectral mass extinction and size and showed considerable variability
- Verification retrievals were performed on measurements of high-purity silica aerosol. The Rayleigh CDE scattering model outperformed Mie theory
- Nonspherical scattering effects can have a significant impact on refractive indices derived from extinction spectra

Correspondence to:
B. E. Reed,
benjamin.reed@physics.ox.ac.uk

Citation:
Reed, B. E., Peters, D. M., McPheat, R., & Grainger, R. G. (2018). The complex refractive index of volcanic ash aerosol retrieved from spectral mass extinction. *Journal of Geophysical Research: Atmospheres*, *123*, 1339–1350. https://doi.org/10.1002/2017JD027362

Received 27 JUN 2017
Accepted 17 DEC 2017
Accepted article online 3 JAN 2018
Published online 29 JAN 2018

Abstract The complex refractive indices of eight volcanic ash samples, chosen to have a representative range of SiO_2 contents, were retrieved from simultaneous measurements of their spectral mass extinction coefficient and size distribution. The mass extinction coefficients, at 0.33–19 μm, were measured using two optical systems: a Fourier transform spectrometer in the infrared and two diffraction grating spectrometers covering visible and ultraviolet wavelengths. The particle size distribution was measured using a scanning mobility particle sizer and an optical particle counter; values for the effective radius of ash particles measured in this study varied from 0.574 to 1.16 μm. Verification retrievals on high-purity silica aerosol demonstrated that the Rayleigh continuous distribution of ellipsoids (CDEs) scattering model significantly outperformed Mie theory in retrieving the complex refractive index, when compared to literature values. Assuming the silica particles provided a good analogue of volcanic ash, the CDE scattering model was applied to retrieve the complex refractive index of the eight ash samples. The Lorentz formulation of the complex refractive index was used within the retrievals as a convenient way to ensure consistency with the Kramers-Kronig relation. The short-wavelength limit of the electric susceptibility was constrained by using independently measured reference values of the complex refractive index of the ash samples at a visible wavelength. The retrieved values of the complex refractive indices of the ash samples showed considerable variation, highlighting the importance of using accurate refractive index data in ash cloud radiative transfer models.

1. Introduction

Even moderately sized explosive volcanic eruptions have the potential to inject many hundreds of megatonnes of volcanic ash into the troposphere and stratosphere. Atmospheric circulation can then transport the ash plume over thousands of kilometers (Watson et al., 2016), intersecting commercial airline routes and posing a significant risk to aviation (Dunn & Wade, 1994; Guffanti et al., 2010). The 2010 Eyjafjallajökull volcanic eruption injected approximately 380 megaton of ash into the atmosphere (Gudmundsson et al., 2012) and cost the global economy an estimated US $5 bn (Oxford Economics, 2010) resulting from the closure of European airspace as the ash plume propagated downwind. In addition to the risk to aviation, there is considerable interest in quantifying the concentrations and dispersal of ash particles, because of their impacts on the climate (Robock, 2000), public health (Horwell & Baxter, 2006), and the environment (Thordarson & Self, 2003). Despite the almost universal assumption within climate models that sulfate aerosol is the only radiatively active volcanic material, it has been found that fine ash particles account for up to 28% of stratospheric volcanic cloud aerosol optical depth 3 months after an eruption (Vernier et al., 2016).

The rapid and accurate detection and quantification of ash using satellites and other remote sensing instruments is vital to mitigate the risks to aviation and better understand plume dispersion dynamics (Prata, 2009). Airborne ash affects atmospheric radiative transfer by scattering solar radiation and by absorbing and emitting infrared radiation; the resulting perturbation to the outgoing top-of-atmosphere radiance can be measured by satellites and used to determine ash plume properties (Grainger et al., 2013). The strong infrared extinction feature of volcanic ash at 8–12 μm, resulting from the absorption of radiation energy exciting $T–O^{-1}$ molecular vibrations (where T indicates fourfold coordinated cations, predominately Si^{4+}, Al^{4+}, and Fe^{3+}) (Di Genova et al., 2015), is widely exploited for the rapid detection of ash using satellites and other remote sensing instruments (Dubuisson et al., 2014; Prata et al., 2016). For example, large negative brightness temperature differences between 10 and 12 μm channels are used by nadir viewing instruments to indicate the presence of ash (Prata, 1989).

The accurate quantification and retrieval of ash plume properties from satellite measurements requires detailed modeling of the radiative transfer through the atmosphere and ash cloud system (Kokhanovsky & de Leeuw, 2009; Ventress et al., 2016). Assumptions in these models, including the complex refractive index of particles, the assumption of spherical particles (and use of Mie theory), and assumptions about the size distribution of particles, propagate to uncertainties in retrieved plume parameters, such as the plume top height, optical path, and the effective radius of ash particles (Corradini et al., 2008; Wen & Rose, 1994; Western et al., 2015).

The scattering and absorption of radiation produced by aerosols varies as a function of the particles' size distribution, complex refractive index, and shape distribution (Bohren & Huffman, 1983); a scattering theory is required to determine the bulk optical properties, such as the volume extinction coefficient and the phase function, from these parameters. In many applications the particles are assumed to be spheres, and Mie theory is used. However, volcanic ash particles formed from explosive fragmentation are known to have highly nonspherical and irregular shapes (Riley et al., 2003). Mie theory provides poor fits to experimental infrared extinction data of silica particles (Bohren & Huffman, 1983; Reed et al., 2017), as well as other nonspherical components of atmospheric mineral dust (Hudson, Gibson, et al., 2008; Hudson, Young, et al., 2008). In the Rayleigh approximation, simple analytic expressions can be derived for the scattering and absorption cross sections of randomly oriented idealized particles shapes (such as disks, needles, and ellipsoids). The extinction predicted by assuming a continuous distribution of ellipsoids (CDEs), in which all geometric shape factors are equally probable, provides a much improved fit to the infrared extinction of crystalline and amorphous silica particles than Mie theory (Bohren & Huffman, 1983; Hudson, Young, et al., 2008; Reed et al., 2017).

Despite the importance of the optical properties of volcanic ash, experimental measurements, over the wavelength range relevant to atmospheric radiative transfer, are extremely limited. In many cases, refractive index data for volcanic pumice determined by Volz (1973), or data for volcanic rocks measured by Pollack et al. (1973), are assumed. This paper presents the mass extinction coefficients (MEC), at 0.33 – 19 μm, and aerolized size distributions of eight volcanic ash samples dispersed in nitrogen gas, measured using a newly developed apparatus detailed in Reed et al. (2017). Additionally, the complex refractive indices of the samples are retrieved from the measured extinction and size distributions, assuming the Rayleigh CDE scattering model.

The paper is structured as follows. Section 2 briefly reviews the experimental apparatus and method. The volcanic ash samples are detailed in section 3. The results for the mass extinction coefficient with uncertainty and size distribution of the samples are presented in section 4. In section 5 the theory of the retrieval of the complex refractive index from extinction data is discussed, including the choice of scattering model and the Lorentz formulation for the complex refractive index. In section 6, it is shown that the Rayleigh CDE scattering model significantly outperforms Mie theory in retrievals of the complex refractive index of crystalline and amorphous silica particles, by comparing to literature values. Assuming that the nonspherical silica particles provide a good analogue of volcanic ash, in section 7 results are presented for the complex refractive index of the volcanic ash samples retrieved from the measured extinction and size distributions, using the Rayleigh CDE scattering model. In section 8 conclusions and future work are outlined.

2. Overview of Experimental Method

Previous mass extinction and size distribution measurements of high-purity crystalline and amorphous silica samples were presented in Reed et al. (2017); the same experimental apparatus and an identical methodology were applied to the eight volcanic ash samples detailed in this paper. In brief, the ash particles were dispersed in Nitrogen gas and passed into a 75 L aerosol cell, in which spectral extinction measurements were performed using two optical systems (The aerosol cell has been described in detail in McPheat et al., 2001.): a Fourier transform spectrometer (FTS) in the infrared (operating at a resolution of 1.9 cm^{-1}) and two diffraction grating spectrometers covering visible and ultraviolet wavelengths (with resolutions of <1.5 nm). The combined spectral range of the extinction measurements was 0.33 – 19 μm. The particle size distribution was measured concurrently using a scanning mobility particle sizer (SMPS), covering particle radii in the range $0.005 < r < 0.44$ μm using 44 logarithmically spaced size bins, and an optical particle counter (OPC), covering $0.15 < r < 10$ μm using 14 logarithmically spaced size bins. Direct mass loading filter measurements were made, allowing the size distributions to be accurately calibrated and providing a high level of confidence in the mass of aerosol per unit volume within the aerosol cell.

Table 1
The Volcanic Ash Samples

Volcano	Eruption date	Bulk SiO_2 wt %
Eyjafjallajökull (a)	5/2011	58.48
Eyjafjallajökull (b)	5/2011	58.03
Askja[a]	1875 layer C	70.65
Nisyros[b]	unknown	69.67
Tongariro	11/2012	59.36
Grimsvötn	5/2011	49.13
Aso	1993	52.55
Spurr[c]	8/1992	

Note. Where possible, references describing how the samples were collected and processed have been included.
[a]Sparks et al. (1981). [b]Longchamp et al. (2011). [c]Harbin et al. (1995).

H_2O and CO_2 gas absorption lines were removed from the extinction spectra, leaving the aerosol extinction component only, by performing gas concentration retrievals using the Reference Forward Model (RFM) (Dudhia, 2017); the in-cell relative humidity could then be determined from the retrieved concentration of H_2O. For a detailed description of the apparatus, experimental method, and the data analysis used to determine the aerosol mass extinction coefficient with uncertainty and size distribution of particles, the reader is referred to Reed et al. (2017).

3. The Volcanic Ash Samples

The eight ash sample used in this work are detailed in Table 1. Previous measurements of the shortwave refractive indices and composition of the samples have been presented in Ball et al. (2015) and Reed (2017). The samples were chosen to include a representative range of SiO_2 contents. The SiO_2 contents given in Table 1 were determined using XRF analysis on the bulk samples; the extent to which this is representative of the very fine fraction measured within the aerosol cell may vary.

4. Mass Extinction Coefficients, Size Distributions, and the In-Cell Relative Humidity

The mass extinction coefficient (MEC), k^{ext} (units: $m^2\ g^{-1}$), is related to the volume extinction coefficient, β^{ext} (units: m^{-1}), and the mass of aerosol per unit volume, ρ_a, according to

$$k^{\text{ext}}(\lambda) = \frac{\beta^{\text{ext}}(\lambda)}{\rho_a}. \quad (1)$$

The mass of aerosol per unit volume was determined from a mass loading filter measurement. The volume extinction coefficient was determined from the measured aerosol transmittance, $T_a(\lambda)$, according to

$$\beta^{\text{ext}} = -\frac{\ln\left(T_a\right)}{x} \quad (2)$$

where is x is the path length of the optical system ($x = 3.52$ m for the FTS measurements and $x = 0.427$ m for the shortwave measurements).

Figure 1 shows the results for the MEC of the eight ash samples with uncertainty. The extinction curves generally show a decrease of extinction with wavelength (0.33–7 μm). The decreasing trend is caused by the reduction in scattering efficiency as the particle size becomes smaller than the wavelength of the incident light. At larger wavelengths (>7 μm) vibrational bands become significant resulting in regions of high extinction due to the absorption of radiation energy within the particles.

In the infrared, all of the samples show a broad absorption feature from approximately 8–12 μm; this feature results from $T-O^-$ vibrations, where T indicates fourfold coordinated cations predominately Si^{4+}, Al^{4+}, and Fe^{3+} (Di Genova et al., 2015). Between the samples there is considerable variation in both the height and breadth of the feature. The peak MEC values, in the infrared, vary from $0.59 \pm 0.13\ m^2\ g^{-1}$ (at 9.90 μm) for Mount Spurr ash to $1.21 \pm 0.065\ m^2\ g^{-1}$ (at 9.58 μm) for the Grímsvötn ash sample. The location of the peak also varies from 9.09 μm for the Nisyros ash to 9.90 μm for the Mount Spurr ash.

Figure 2 shows the results for the in-cell size distribution of the ash samples. The size distributions were calculated as detailed in Reed et al. (2017), with the dilution between the aerosol cell accurately calibrated using a mass loading filter measurement. A dynamic shape factor of $\chi = 1.0$ was assumed for all of the ash samples; this is consistent with measurements of similarly sized silica particles performed by Hudson, Young, et al. (2008). It can be seen that there is good agreement between the SMPS and OPC in their overlap region. The SMPS and OPC data were combined into a single size distribution for use in the refractive index retrievals by using SMPS data up to the instrument's largest size bin and using OPC data for larger radii. Table 2 details values of the effective radius, r_e, determined from the in-cell size distributions (The effective radius, r_e, is defined as the ratio of the third moment of the size distribution to the second moment of the size distribution.). It can be seen that there is a considerable degree of variation in value of the effective radius, which vary from a value

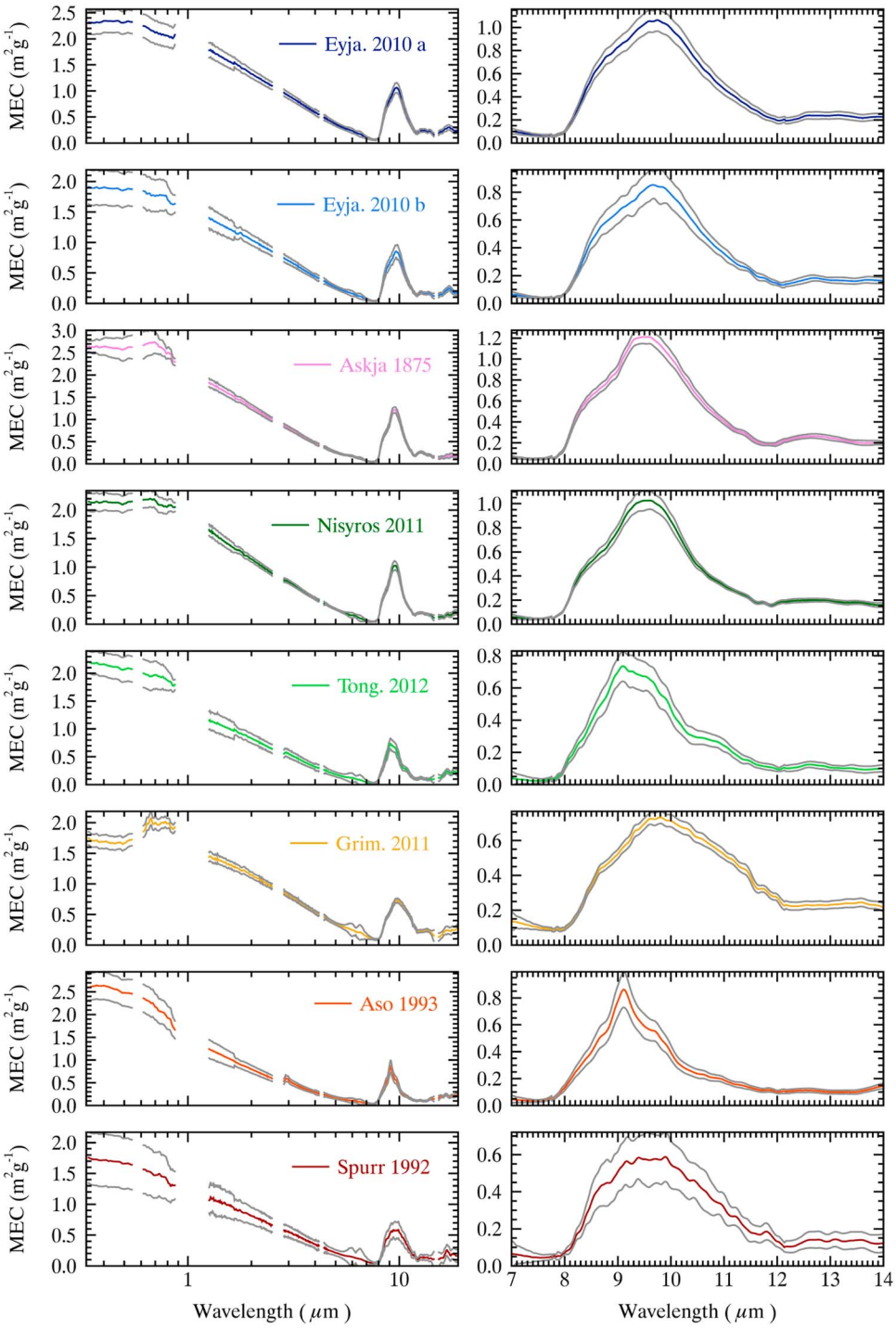

Figure 1. Results for the mass extinction coefficient (MEC) of the eight ash sample with one-sigma uncertainty indicated in gray.

of 0.574 μm for the Aso ash to a value of 1.16 μm for Nisyros ash; these differences derive largely from differences in the large-particle tail of the distributions which are not immediately apparent in the distribution plots of Figure 2.

Table 2 shows results for various in-cell parameters. The concentrations of H_2O and CO_2 gases, in parts per million by volume (ppmv), were determined from gas line retrievals using the RFM (Dudhia, 2017); the concentration of H_2O and the in-cell pressure was used to determine the in-cell relative humidity, RH. Additionally,

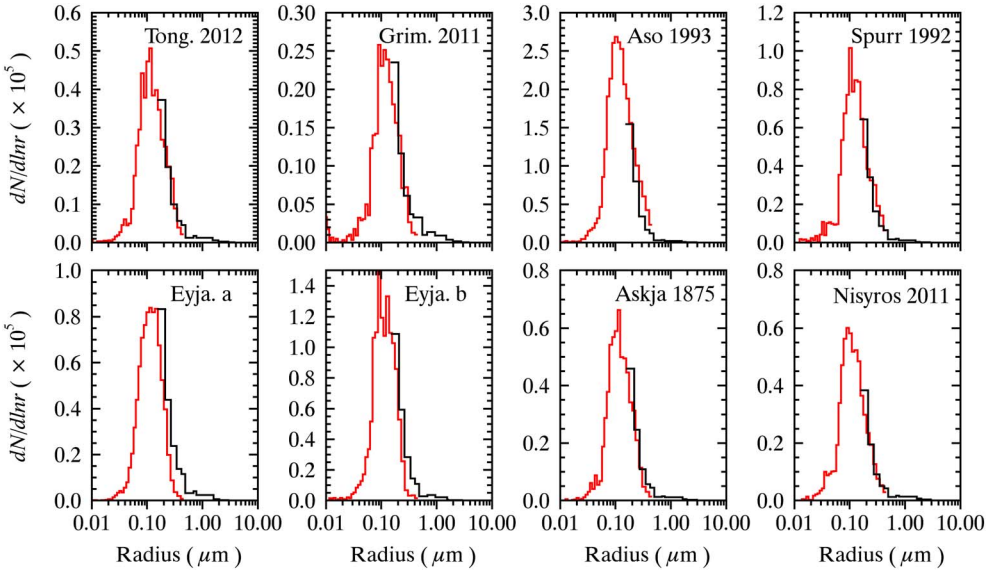

Figure 2. The in-cell size distributions of the eight ash samples. The SMPS measurements are plotted in red, while the OPC measurements are shown in black. The plots show $dN/dlnr$ where N has units of particles per cm^3.

the mass of aerosol per unit volume, ρ_a, with uncertainty, determined from the mass loading filter measurement and accurate filter flow rate measurements. For a detailed account on how these parameters were determined, see Reed et al. (2017).

5. Retrieval of the Complex Refractive Index: Theory

5.1. The Choice of Scattering Model

A scattering theory is required to model the extinction produced by the aerosol particles. The volume extinction coefficient, β^{ext}, can be expressed as follows:

$$\beta^{ext} = \int_0^\infty \sigma^{ext} n(r) \mathrm{d}r, \tag{3}$$

where $n(r)\mathrm{d}r$ is the number of particles per unit volume with radii between r and $r+\mathrm{d}r$, and σ^{ext} is the extinction cross section which, in general, is a function of the particle complex refractive index, $m(\lambda) = n+i\kappa$, the particle size parameter, $x = 2\pi r/\lambda$, and the particle shape. The extinction cross section can be expressed in terms of the absorption and scattering cross sections:

$$\sigma^{ext} = \sigma^{abs} + \sigma^{sca}. \tag{4}$$

Table 2
In-cell Parameters: The Mass of Aerosol Per Unit Volume, ρ_a; The Effective Radius, r_e, of Particles; The Retrieved Concentrations of CO_2 and H_2O; and the Relative Humidity

Sample	ρ_a ($\times 10^{-2}$ g m^{-3})	Effective radius (μm)	CO_2 (ppmv)	H_2O (ppmv)	RH (%)
Eyjafjallajökull (a)	5.85 ± 0.13	0.856	261 ± 4	684 ± 1	0.276
Eyjafjallajökull (b)	5.58 ± 0.14	0.758	242 ± 4	502 ± 1	0.202
Askja	4.43 ± 0.14	1.04	257 ± 1	637 ± 1	0.257
Nisyros	5.83 ± 0.14	1.16	230 ± 4	464 ± 1	0.187
Tongariro	4.93 ± 0.09	1.05	255 ± 5	543 ± 1	0.219
Grimsvötn	3.17 ± 0.11	1.10	256 ± 3	467 ± 1	0.188
Aso	8.41 ± 0.09	0.574	243 ± 6	484 ± 1	0.195
Spurr	3.49 ± 0.35	0.612	157 ± 4	417 ± 1	0.168

Mie theory describes the exact solution to the electromagnetic scattering produced by a sphere. The Mie extinction cross section is expressed in terms of the infinite series:

$$\sigma_{\text{Mie}}^{\text{ext}} = \frac{\lambda^2}{2\pi}\sum_{n=0}^{\infty}(2n+1)\text{Re}\left[a_n(m,x)+b_n(m,x)\right], \tag{5}$$

where $a_n(m,x)$ and $b_n(m,x)$ are the scattering coefficients that depend on the complex refractive index and the size parameter and are expressed in terms of the Ricatti-Bessel functions.

It has been found that assuming spheres and using Mie theory poorly models the infrared extinction features of fine crystalline and amorphous silica particles, and the Rayleigh CDE model provides much improved fits to experimental data (Bohren & Huffman, 1983; Hudson, Young, et al., 2008; Reed et al., 2017). In the Rayleigh approximation ($x \ll 1$), it can be shown that the absorption and scattering cross sections for a continuous distribution of ellipsoids (CDE), in which all shape factors are equally probable, can be expressed as (Bohren & Huffman, 1983; Min & Hovenier, 2003)

$$\sigma_{\text{CDE}}^{\text{abs}} = k\,V\,\text{Im}\left[\frac{2m^2}{m^2-1}\ln\left(m^2\right)\right], \tag{6}$$

$$\sigma_{\text{CDE}}^{\text{sca}} = \frac{k^4\,V^2\,\left|m^2-1\right|}{3\pi\,\text{Im}\left(m^2\right)}\,\text{Im}\left[\frac{2m^2}{m^2-1}\ln\left(m^2\right)\right], \tag{7}$$

where $k = 2\pi/\lambda$ is the wave number, $V = \frac{4}{3}\pi r_{ve}^3$ is the volume of particles, and $\ln(z)$ denotes the principle logarithm of z.

5.2. The Lorentz Formulation of the Complex Refractive Index

The retrieval problem is underconstrained because at each wavelength there is one measurement of extinction and two unknowns: the real and the imaginary refractive index. One possibility is to use the Kramers-Kronig (KK) relation between the real and imaginary refractive index (Bohren & Huffman, 1983):

$$n(\omega) - 1 = \frac{2}{\pi}P\int_0^{\infty}\frac{\Omega\kappa(\omega)}{\Omega^2-\omega^2}\text{d}\Omega \tag{8}$$

where ω is the angular frequency of light ($\omega = 2\pi c/\lambda$) and P is the principle value of the Cauchy integral. The KK relation allows the real refractive index to be determined from the imaginary refractive index and vice versa; thus, the retrieval problem becomes well constrained. However, the practical application of the KK relation poses problems because the integral requires κ (or n) to be known over an infinite angular frequency interval.

As outlined in Thomas et al. (2005), a convenient approach is to use the Lorentz harmonic oscillator model of the electric susceptibility; the model guarantees that the KK relation is obeyed. The Lorentz model expresses the real and imaginary parts of the electric susceptibility, ϵ_{r} and ϵ_{i}, in terms of J oscillators (or bands):

$$\epsilon_{\text{r}}(\omega) = \epsilon_{\infty} + \sum_{j=1}^{J}\frac{S_j\left(\omega_j^2-\omega^2\right)}{\left(\omega_j^2-\omega^2\right)^2+\gamma_j^2\omega_j^2}, \tag{9}$$

$$\epsilon_{\text{i}}(\omega) = \sum_{j=1}^{J}\frac{S_j\gamma_j\omega}{\left(\omega_j^2+\omega^2\right)^2+\gamma^2\omega_j^2}, \tag{10}$$

where ω_j is the resonant angular frequencies of the bands, S_j is the band strength parameters, γ_j is the damping constants, and ϵ_{∞} is the electric susceptibility in the short-wavelength (high-frequency) limit. The real and imaginary parts of the refractive index can be expressed in terms of ϵ_{r} and ϵ_{i}:

$$n(\omega) = \left\{\frac{1}{2}\left[\sqrt{\epsilon_{\text{r}}(\omega)^2+\epsilon_{\text{i}}(\omega)^2}+\epsilon_{\text{r}}(\omega)\right]\right\}^{1/2}, \tag{11}$$

$$\kappa(\omega) = \left\{\frac{1}{2}\left[\sqrt{\epsilon_{\text{r}}(\omega)^2+\epsilon_{\text{i}}(\omega)^2}-\epsilon_{\text{r}}(\omega)\right]\right\}^{1/2}. \tag{12}$$

In order to constrain the value of ϵ_{∞} within the retrievals, reference values for the complex refractive index of the ash samples at 450.0 nm were used. The values used for the shortwave reference refractive indices were

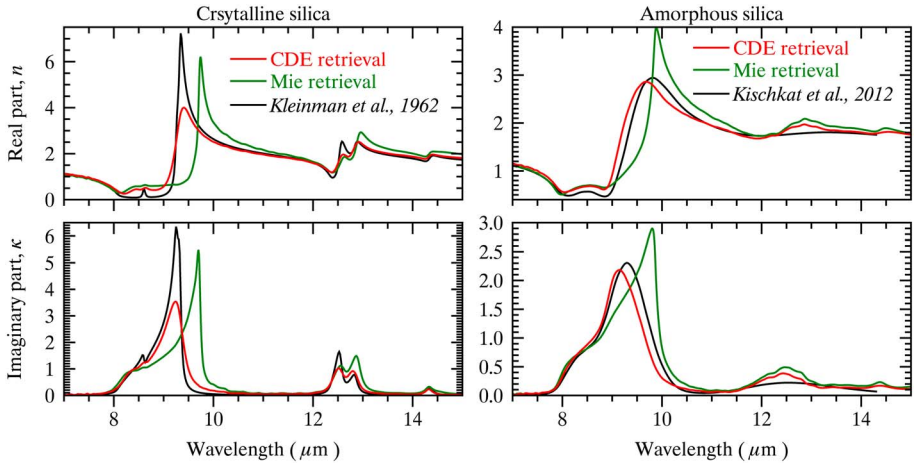

Figure 3. The complex refractive index of high-purity crystalline and amorphous silica samples retrieved from their mass extinction coefficients and size distributions. The retrieval results are shown using two different scattering models: Mie theory (green) and the Rayleigh CDE model (red). Literature values of the complex refractive index are shown in black.

published in Ball et al. (2015) and Reed (2017); the earlier work used identical ash samples to those detailed in this paper and determined their complex refractive index at visible wavelengths. The reference values are used to constrain ϵ_∞ by noting that

$$\epsilon_r = n^2 - \kappa^2, \tag{13}$$

such that

$$\epsilon_\infty = n_{\text{Ref}}^2 - \kappa_{\text{Ref}}^2 - \sum_{j=1}^{J} \frac{S_j\left(\omega_j^2 - \omega_{\text{Ref}}^2\right)}{\left(\omega_j^2 - \omega_{\text{Ref}}^2\right)^2 + \gamma_j \omega_{\text{Ref}}^2}, \tag{14}$$

where n_{Ref} and κ_{Ref} are the real and imaginary parts of the reference refractive index, and ω_{Ref} is the angular frequency of these measured values.

The approach of using measured values of the shortwave complex refractive index to constrain ϵ_∞ has significant advantages over other work. For example, Di Biagio et al. (2014) resorted to manually adjusting ϵ_∞. Relatively small adjustments to ϵ_∞ can lead to significant changes in the retrieved infrared band parameters, necessitating the use of independently measured shortwave refractive indices.

6. Retrieval Verification: Silica Aerosol

The mass extinction and size distribution measurements used for the silica verification retrievals were presented in Reed et al. (2017). Following the retrieval approach outlined in Thomas et al. (2005), the Levenberg-Marquardt method was used to search for the set of band parameters that best fit the experimental extinction spectra, keeping the measured size distribution of particles fixed within the retrievals and using the reference shortwave refractive indices to constrain ϵ_∞ according to equation (14) (See, e.g., Rodgers, 2000.).

Separate retrievals were performed using two scattering models: Mie theory (for spherical particles) and the Rayleigh CDE model. The retrievals were performed over the wavelength range 7–15 μm and were initialized using 367 bands evenly spaced by wave number. The retrievals were restricted to wavelengths 7–15 μm for the following reasons: at wavelengths >15 μm the measurement uncertainty increased to levels comparable to the measured extinction; at wavelength <7 μm the Rayleigh approximation for the particles begins to break down (Reed et al., 2017); and finally, aerosol absorption bands are not expected in the shortwave.

Figure 3 shows the results for the retrieved complex refractive index of particles (determined from the retrieved band parameters) using the two scattering models; the Mie retrieval is shown in green, while the Rayleigh CDE retrieval is shown in red. Plotted in black are literature values of the complex refractive indices: for amorphous silica the values measured by Kischkat et al. (2012) are shown; for crystalline silica the weighted averages of the ordinary and extraordinary components, $m = \frac{2}{3}m_o + \frac{1}{3}m_e$, determined by Kleinman and Spitzer (1962) are shown.

It can be seen that for both the crystalline and amorphous samples, the CDE retrieval compares remarkably well with the literature values, while the Mie retrieval produces refractive index features that are significantly shifted toward larger wavelengths compared to the literature values. For the amorphous case, the R^2 value between the literature refractive index and the Mie retrieval are 0.80 and 0.76 for the real and imaginary parts; this compares to values of 0.95 and 0.94 for the CDE model. For the crystalline case, R^2 values are 0.25 and 0.21 for the real and imaginary parts of the Mie retrieved refractive index compared to literature values; while the values for the CDE retrieval are 0.91 and 0.92. These results should come as no surprise, given that the CDE model is known to significantly outperform Mie theory in forward modeling the extinction spectra of silica particles (Bohren & Huffman, 1983; Hudson, Young, et al., 2008; Reed et al., 2017). The results clearly demonstrate that refractive indices derived from extinction spectra assuming Mie scattering must be treated with a great deal of caution when the particles are known to have a significant degree of nonsphericity. Furthermore, band features shifted to longer wavelengths appear to be characteristic of failing to account for spherical effects. For example, the peak in the retrieved imaginary refractive index of amorphous silica determined assuming Mie scattering is shifted to longer wavelengths by 0.65 μm compared to the CDE value.

7. Ash Complex Refractive Index Results and Discussion

Based on the results for silica aerosol presented above, and assuming that amorphous silica provides a good analogue of volcanic ash, the Rayleigh CDE model was applied to retrieve the complex refractive index of the ash samples. Volcanic ash has silica content varying from 50 to 75% (Cashman & Rust, 2016); the silica is quenched within amorphous fragments of volcanic glass. While amorphous silica consists of disordered networks of SiO_4 tetrahedra, volcanic glass consists predominately of disordered networks of TO_4 tetrahedra (where T indicates fourfold coordinated cations, mainly Si^{4+}, Al^{3+}, and Fe^{3+}). Given these molecular and structural similarities, it may not be unreasonable to assume that volcanic ash fragments have similar properties to amorphous silica fragments, including shape. Furthermore, scanning electron microscopy (SEM) images of silica and quartz particles (Balduzzi et al., 2004; Veghte et al., 2016) show similar irregular particle shapes to SEM images of volcanic ash fragments (Gislason et al., 2011).

Figure 4 shows the results for the retrieved complex refractive index of the samples. There is a considerable variation in the retrieved refractive indices between the samples, although some spectral regions have higher variability than others. The peak in the imaginary refractive between 8–12 μm results from the absorption of radiation energy exciting $T-O^{-1}$ vibrations (where T indicates fourfold coordinated cations); these vibrations also cause the minima followed by maxima seen in the real refractive indices of the samples. From 8 to 9 μm there is relatively little variation in the imaginary refractive index between the samples, while at larger wavelengths the variability increases. The peak in the imaginary refractive index of the samples varies from a value of 0.64 for the Mount Tongariro ash to a value of 1.05 for the Eyjafjallajökull (b) ash sample. The location of the peak varies from 9.09 μm for Mount Tongariro ash to 9.99 μm for Grímsvötn ash. There is also considerable variation in the breadth of the peak, with Grímsvötn ash showing the broadest feature and Mount Aso ash displaying the narrowest peak.

The retrieved imaginary refractive index of the two Eyjafjallajökull samples is almost identical up to approximately 11 μm but differs slightly at larger wavelengths. The real refractive index of the two samples is similar; however, Eyjafjallajökull (b) is slightly lower than sample (a). Although SEM Bulk compositional analysis of the samples shows similar compositions, with Eyjafjallajökull (a) and (b) having SiO_2 contents of 58.48 and 58.03 wt %, these measurements were performed on the bulk sample rather than the very fine component measured in the aerosol cell. It is therefore still possible that there was some variation in the composition of the fine fraction of the samples. However, it is also possible that uncertainties in the measured size distributions may have played a role in the differences. In order to investigate the sensitivity of retrieved complex refractive index to uncertainty in the measured size distribution a Monte Carlo analysis was performed. A Gaussian random error of 5% was added to each bin of the size distribution, the retrieval of complex refractive index using the CDE model was performed and this process was repeated 50 times (the analysis was performed using the Aso ash experimental data). The standard deviation in values of the retrieved refractive index was found to be less than 0.02 (approximately 2%) for the real part and less than 0.03 (approximately 4%) for the imaginary part, in the wavelength range 7–13 μm. Although the sensitivity to random error in the size distribution is relatively low, it is possible that systematic errors were more significant. The scattering component of the extinction is particularly sensitive to the large-particle tail of the distribution measured by the OPC. The OPC

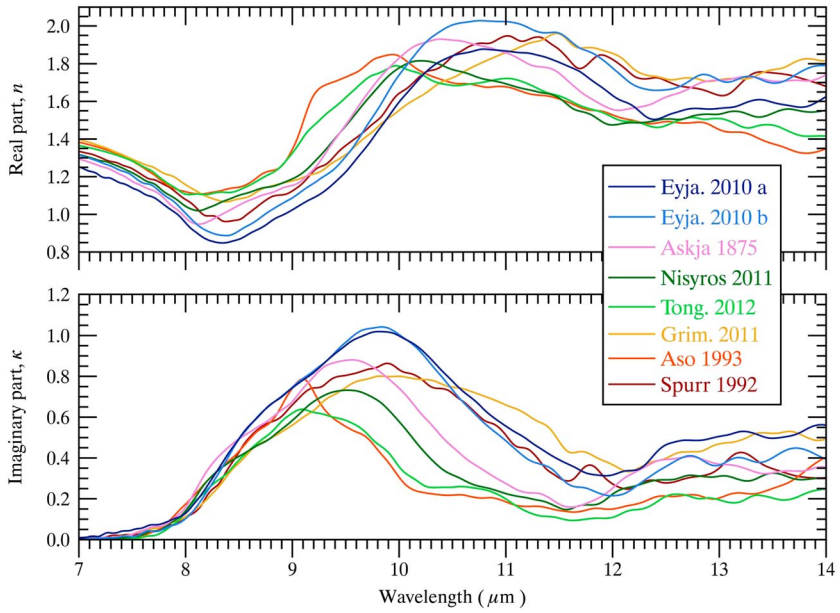

Figure 4. The complex refractive indices of the ash samples retrieved from their extinction spectra and size distributions, assuming the Rayleigh CDE scattering model.

uses Mie theory to invert the measured scattered intensity at 780 nm to determine particle radius. Therefore, nonspherical scattering effects will introduce systematic error into the distribution returned by the OPC.

A significant assumption of the approach adopted is that the Rayleigh CDE model provides a good description of the nonspherical scattering of very fine volcanic ash particles; this was motivated by the results for silica aerosol where the CDE model significantly outperformed Mie theory in retrieving the complex refractive index (as judged by comparing to literature refractive indices). However, it is quite possible that the shape of the ash particles varied between the samples and source volcanoes, and these differences would not be reflected by the scattering model. More work is required to investigate the nonspherical light scattering properties of volcanic ash particles and to determine the associated uncertainties in the retrieval of the complex refractive index from extinction data when a particular scattering model is assumed.

8. Conclusions and Suggested Future Work

This paper presents the mass extinction coefficients, at 0.33–19 μm, and size distributions of eight volcanic ash samples, measured using newly developed apparatus detailed in Reed et al. (2017). The complex refractive indices of the samples have been retrieved from the extinction and size distribution measurements, assuming the Rayleigh CDE scattering model. The choice of scattering model was motivated by verification retrievals performed on high-purity silica aerosol; the Rayleigh CDE model significantly outperformed Mie theory in retrieving the complex refractive index, evaluated by comparing to literature values. The results for the complex refractive index of the samples show considerable variation between the samples, which highlights the importance of accurate refractive index data when modeling radiative transfer within ash clouds.

Although there was considerable variation in values of the peak imaginary refractive index and in the breadth of the feature associated with $T-O^{-1}$ vibrations, the variability was much lower in the spectral region 8–9 μm compared to longer wavelengths. It appears that the imaginary refractive index is less sensitive to differences in composition between 8 and 9 μm. This region might therefore be useful in remote sensing applications, for example, in determining the columnar concentration of ash when its refractive index is unknown. Furthermore, the region 9–12 μm has high variability and might be useful in providing information about the composition of the samples from remote sensing measurements.

The Lorentz formulation was used to represent the complex refractive index of the samples; the approach provides a convenient way to parameterize the retrieved refractive index, ensuring it is consistent with the Kramers-Kronig relation and reducing the number of retrieved parameters so that the retrieval problem is no

longer underconstrained. Reference values for the complex refractive indices of the ash samples in the visible, presented in Ball et al. (2015) and Reed (2017), were used to constrain the value of ϵ_∞. This approach represents a significant improvement over work by others where the value has been manually adjusted, because small adjustments to ϵ_∞ can cause changes in the retrieved infrared bands.

As presented in section 6, the differences between the retrieved refractive index of silica, when the Rayleigh CDE model is used compared to when Mie theory is assumed, are significant. The results demonstrate that failing to account for nonspherical scattering effects can have a significant impact on refractive indices retrieved from extinction spectra; it appears that retrieved infrared bands that are shifted toward longer wavelengths are characteristic of such a failure. More work is required to quantify the uncertainties in refractive indices derived from extinction spectra resulting from shape assumptions in the scattering model.

A significant hypothesis of the work presented in this paper is that the Rayleigh CDE model provides a good approximation to the nonspherical scattering of the very fine component of the volcanic ash that was measured in the aerosol cell. This hypothesis was supported by the silica results and the assumption that the silica particle provides a good analogue of volcanic ash; SEM images of volcanic ash and silica particles qualitatively show similarities, with highly irregular particle shapes. However, it is quite possible that the shape of the ash fragments varied between the samples, perhaps due to differences in the volcanic fragmentation process; these differences would not be reflected by the scattering model. Further work is needed to investigate the nonspherical scattering properties of volcanic ash fragments, investigating which models most accurately forward model bulk optical properties such as the extinction coefficient.

The applicability of the Rayleigh CDE model is limited to particles that are small compared to the radiation wavelength; the Rayleigh approximation held for the particles measured in the aerosol cell and presented in this paper but might not hold for similar measurements on larger particles. It is possible that *T*-matrix methods (Mishchenko et al., 1996; Waterman, 1971), applying a distribution of spheroidal shapes, might be an appropriate approximation for larger particles; the approach is used within the remote sensing of atmospheric desert dust (Dubovik et al., 2006; Mishchenko et al., 1997) and can match light scattering data of a range of nonspherical components of mineral dust including silica particles (Kleiber et al., 2009; Nousiainen et al., 2006; Reed et al., 2017). However, the *T*-matrix calculations can fail to converge for large and highly eccentric particles (Mishchenko & Travis, 1998), which may pose problems in the application to larger volcanic ash particles.

Acknowledgments
This study was funded as part of NERC's support of the National Centre for Earth Observation. R. G. G. was supported by the NERC VANAHEIM project NE/1015592/1, the NERC SHIVA project NE/J023310/1, and the NERC Centre for Observation and Modelling of Earthquakes, Volcanoes, and Tectonics (COMET). B. E. R. was funded by a NERC studentship NE/J500045/1. The complex refractive index data presented within this paper are available at http://eodg.atm.ox.ac.uk/ARIA/index.html. Other data used in the paper are available upon request from the author.

References

Balduzzi, M., Diociaiuti, M., Berardis, B. D., Paradisi, S., & Paoletti, L. (2004). In vitro effects on macrophages induced by noncytotoxic doses of silica particles possibly relevant to ambient exposure. *Environmental Research*, *96*(1), 62–71. https://doi.org/10.1016/j.envres.2003.11.004

Ball, J. G. C., Reed, B. E., Grainger, R. G., Peters, D. M., Mather, T. A., & Pyle, D. M. (2015). Measurements of the complex refractive index of volcanic ash at 450, 546.7, and 650 nm. *Journal of Geophysical Research: Atmospheres*, *120*, 7747–7757. https://doi.org/10.1002/2015JD023521

Bohren, C. F., & Huffman, D. R. (1983). *Absorption and scattering of light by small particles*. New York: John Wiley.

Cashman, K., & Rust, A. (2016). Introduction. In Cashman, K., & Rust, A. (Eds.), *Volcanic Ash* (pp. 5–22). Amsterdam: Elsevier. https://doi.org/10.1016/B978-0-08-100405-0. 00002-1

Corradini, S., Spinetti, C., Carboni, E., Tirelli, C., Buongiorno, M. F., Pugnahi, S., & Gangale, G. (2008). Mt. Etna tropospheric ash retrieval and sensitivity analysis using moderate resolution imaging spectroradiometer measurements. *Journal of Applied Remote Sensing*, *2*(1), 023550. https://doi.org/10.1117/1.3046674

Di Biagio, C., Formenti, P., Styler, S. A., Pangui, E., & Doussin, J.-F. (2014). Laboratory chamber measurements of the longwave extinction spectra and complex refractive indices of African and Asian mineral dusts. *Geophysical Research Letters*, *41*, 6289–6297. https://doi.org/10.1002/2014GL060213

Di Genova, D., Morgavi, D., Hess, K.-U., Neuville, D. R., Borovkov, N., Perugini, D., & Dingwell, D. B. (2015). Approximate chemical analysis of volcanic glasses using Raman spectroscopy. *Journal of Raman Spectroscopy*, *46*(12), 1235–1244. https://doi.org/10.1002/jrs.4751

Dubovik, O., Sinyuk, A., Lapyonok, T., Holben, B. N., Mishchenko, M., Yang, P., … Slutsker, I. (2006). Application of spheroid models to account for aerosol particle nonsphericity in remote sensing of desert dust. *Journal of Geophysical Research*, *111*, D11208. https://doi.org/10.1029/2005JD006619

Dubuisson, P., Herbin, H., Minvielle, F., Compiègne, M., Thieuleux, F., Parol, F., & Pelon, J. (2014). Remote sensing of volcanic ash plumes from thermal infrared: A case study analysis from SEVIRI, MODIS and IASI instruments. *Atmospheric Measurement Techniques*, *7*(2), 359–371. https://doi.org/10.5194/amt-7-359-2014

Dudhia, A. (2017). The reference forward model (RFM). *Journal of Quantitative Spectroscopy and Radiative Transfer*, *186*, 243–253. https://doi.org/10.1016/j.jqsrt.2016.06.018

Dunn, M. G., & Wade, D. P. (1994). Influence of volcanic ash clouds on gas turbine engines. In T. J. Casadevall (Ed.), *Proceedings of the first international symposium on volcanic ash and aviation safety* (pp. 107–117). Washington: USGS Bulletin 2047.

Gislason, S. R., Hassenkam, T., Nedel, S., Bovet, N., Eiriksdottir, E. S., Alfredsson, H. A., … Stipp, S. L. S. (2011). Characterization of Eyjafjallajökull volcanic ash particles and a protocol for rapid risk assessment. *Proceedings of the National Academy of Sciences*, *108*(18), 7307–7312. https://doi.org/10.1073/pnas.1015053108

Grainger, R. G., Peters, D. M., Thomas, G. E., Smith, A. J. A., Siddans, R., Carboni, E., & Dudhia, A. (2013). Measuring volcanic plume and ash properties from space. In *Remote sensing of volcanoes and volcanic processes: Integrating observation and modelling Geological Society London, Special Publications*, *380*, 293–320. https://doi.org/10.1144/SP380.7

Gudmundsson, M. T., Thordarson, T., Höskuldsson, Ármann, Larsen, G., Björnsson, H., & Prata, F. J. (2012). Ash generation and distribution from the April–May 2010 eruption of Eyjafjallajökull, Iceland. *Scientific Reports*, *2*, 572. https://doi.org/10.1038/srep00572

Guffanti, M., Casadevall, T. J., & Budding, K. (2010). Encounters of aircraft with volcanic ash clouds: A compilation of known incidents, 1953–2009 (Technical Report). Reston, Virginia: U.S. Geological Survey.

Harbin, M., Swanson, S., Nye, C., & Miller, T. (1995). Preliminary petrology and chemistry of proximal eruptive products; 1992 eruptions of Crater Peak, Mount Spurr Volcano, Alaska. In T. Keith (Ed.), *The 1992 eruptions of Crater Peak vent, Mount Spurr Volcano, Alaska. U.S. Geological Survey Professional Paper*, 139–148.

Horwell, C. J., & Baxter, P. J. (2006). The respiratory health hazards of volcanic ash: A review for volcanic risk mitigation. *Bulletin of Volcanology*, *69*(1), 1–24. https://doi.org/10.1007/s00445-006-0052-y

Hudson, P. K., Gibson, E. R., Young, M. A., Kleiber, P. D., & Grassian, V. H. (2008). Coupled infrared extinction and size distribution measurements for several clay components of mineral dust aerosol. *Journal of Geophysical Research*, *113*, D01201. https://doi.org/10.1029/2007JD008791

Hudson, P. K., Young, M. A., Kleiber, P. D., & Grassian, V. H. (2008). Coupled infrared extinction spectra and size distribution measurements for several non-clay components of mineral dust aerosol (quartz, calcite, and dolomite). *Atmospheric Environment*, *42*(24), 5991–5999. https://doi.org/10.1016/j.atmosenv.2008.03.046

Kischkat, J., Peters, S., Gruska, B., Semtsiv, M., Chashnikova, M., Klinkmüller, M., … Masselink, W. T. (2012). Mid-infrared optical properties of thin films of aluminum oxide, titanium dioxide, silicon dioxide, aluminum nitride, and silicon nitride. *Applied Optics*, *51*(28), 6789–6798. https://doi.org/10.1364/AO.51.006789

Kleiber, P. D., Grassian, V. H., Young, M. A., & Hudson, P. K. (2009). *T*-matrix studies of aerosol particle shape effects on IR resonance spectral line profiles and comparison with an experiment. *Journal of Geophysical Research*, *114*, D21209. https://doi.org/10.1029/2009JD012710

Kleinman, D. A., & Spitzer, W. G. (1962). Theory of the optical properties of quartz in the infrared. *Physical Review*, *125*, 16–30. https://doi.org/10.1103/PhysRev.125.16

Kokhanovsky, A. A., & de Leeuw, G. (2009). *Satellite aerosol remote sensing over land*. Chichester, UK: Springer, Paris.

Longchamp, C., Bonadonna, C., Bachmann, O., & Skopelitis, A. (2011). Characterization of tephra deposits with limited exposure: The example of the two largest explosive eruptions at Nisyros volcano (Greece). *Bulletin of Volcanology*, *73*(9), 1337–1352. https://doi.org/10.1007/s00445-011-0469-9

McPheat, R. A., Newnham, D. A., Williams, R. G., & Ballard, J. (2001). Large-volume, coolable spectroscopic cell for aerosol studies. *Applied Optics*, *40*(36), 6581–6586. https://doi.org/10.1364/AO.40.006581

Min, M., & Hovenier, J. W. (2003). Shape effects in scattering and absorption by randomly oriented particles small compared to the wavelength. *Astronomy and Astrophysics*, *404*(1), 35–46. https://doi.org/10.1051/0004-6361: 20030456

Mishchenko, M. I., & Travis, L. D. (1998). Capabilities and limitations of a current FORTRAN implementation of the *T*-matrix method for randomly oriented, rotationally symmetric scatterers. *Journal of Quantitative Spectroscopy and Radiative Transfer*, *60*, 309–324. https://doi.org/10.1016/S0022-4073(98)00008-9

Mishchenko, M. I., Travis, L. D., Kahn, R. A., & West, R. A. (1997). Modeling phase functions for dustlike tropospheric aerosols using a shape mixture of randomly oriented polydisperse spheroids. *Journal of Geophysical Research*, *102*(D14), 16,831–16,847. https://doi.org/10.1029/96JD02110

Mishchenko, M. I., Travis, L. D., & Mackowski, D. W. (1996). *T*-matrix computations of light scattering by nonspherical particles: A review. *Journal of Quantitative Spectroscopy and Radiative Transfer*, *55*(5), 535–575. https://doi.org/10.1016/0022-4073(96)00002-7

Nousiainen, T., Kahnert, M., & Veihelmann, B. (2006). Light scattering modeling of small feldspar aerosol particles using polyhedral prisms and spheroids. *Journal of Quantitative Spectroscopy and Radiative Transfer*, *101*(3), 471–487. https://doi.org/10.1016/j.jqsrt.2006.02.038

Oxford Economics (2010). The economic impacts of air travel restrictions due to volcanic ash (Report) (p. 12). Oxford, UK: Abbey House.

Pollack, J. B., Toon, O. B., & Khare, B. N. (1973). Optical properties of some terrestrial rocks and glasses. *Icarus*, *19*(3), 372–389. https://doi.org/10.1016/0019-1035(73)90115-2

Prata, A. J. (1989). Observations of volcanic ash clouds in the 10–12 μm window using AVHRR/2 data. *International Journal of Remote Sensing*, *10*, 751–761.

Prata, A. J. (2009). Satellite detection of hazardous volcanic clouds and the risk to global air traffic. *Natural Hazards*, *51*(2), 303–324. https://doi.org/10.1007/s11069-008-9273-z

Prata, A. J., Dezitter, F., Davies, I., Weber, K., Birnfeld, M., Moriano, D., … Weber, M. (2016). Artificial cloud test confirms volcanic ash detection using infrared spectral imaging. *Scientific Reports*, *6*, 25620.

Reed, B. E. (2017). Measurements of the complex refractive index of volcanic ash (PhD thesis). Oxford: University of Oxford.

Reed, B. E., Peters, D. M., McPheat, R., Smith, A. J., & Grainger, R. (2017). Mass extinction spectra and size distribution measurements of quartz and amorphous silica aerosol at 0.33–19 μm compared to modelled extinction using Mie, CDE, and T-matrix theories. *Journal of Quantitative Spectroscopy and Radiative Transfer*, *199*, 52–65. https://doi.org/10.1016/j.jqsrt.2017.05.011

Riley, C. M., Rose, W. I., & Bluth, G. J. S. (2003). Quantitative shape measurements of distal volcanic ash. *Journal of Geophysical Research*, *108*(B10), 2504. https://doi.org/10.1029/2001JB000818

Robock, A. (2000). Volcanic eruptions and climate. *Reviews of Geophysics*, *38*(2), 191–219. https://doi.org/10.1029/1998RG000054

Rodgers, C. D. (2000). *Inverse methods for atmospheric sounding: Theory and practice*. Singapore: World Scientific Co. Pte. Ltd.

Sparks, R. S. J., Wilson, L., & Sigurdsson, H. (1981). The pyroclastic deposits of the 1875 eruption of Askja, Iceland. *Philosophical Transactions of the Royal Society of London A: Mathematical, Physical and Engineering Sciences*, *299*(1447), 241–273. https://doi.org/10.1098/rsta.1981.0023

Thomas, G. E., Bass, S. F., Grainger, R. G., & Lambert, A. (2005). Retrieval of aerosol refractive index from extinction spectra with a damped harmonic-oscillator band model. *Applied Optics*, *44*(7), 1332–1341. https://doi.org/10.1364/AO.44.001332

Thordarson, T., & Self, S. (2003). Atmospheric and environmental effects of the 1783–1784 Laki eruption: A review and reassessment. *Journal of Geophysical Research*, *108*(D1), 4011. https://doi.org/10.1029/2001JD002042

Veghte, D. P., Altaf, M. B., Haines, J. D., & Freedman, M. A. (2016). Optical properties of non-absorbing mineral dust components and mixtures. *Aerosol Science and Technology*, *50*(11), 1239–1252. https://doi.org/10.1080/02786826.2016.1225153

Ventress, L. J., McGarragh, G., Carboni, E., Smith, A. J., & Grainger, R. G. (2016). Retrieval of ash properties from IASI measurements. *Atmospheric Measurement Techniques*, *9*(11), 5407–5422. https://doi.org/10.5194/amt-9-5407-2016

Vernier, J.-P., Fairlie, T. D., Deshler, T., Natarajan, M., Knepp, T., Foster, K., … Trepte, C. (2016). In situ and space-based observations of the Kelud volcanic plume: The persistence of ash in the lower stratosphere. *Journal of Geophysical Research: Atmospheres*, *121*, 11,104–11,118. https://doi.org/10.1002/2016JD025344

Volz, F. E. (1973). Infrared optical constants of ammonium sulfate, Sahara dust, volcanic pumice and flyash. *Applied Optics*, *12*, 564–568.

Waterman, P. C. (1971). Symmetry, unitarity, and geometry in electromagnetic scattering. *Physical Review D: Covering Particles, Fields, Gravitation, and Cosmology*, *3*, 825–839. https://doi.org/10.1103/PhysRevD.3.825

Watson, E. J., Swindles, G. T., Stevenson, J. A., Savov, I., & Lawson, I. T. (2016). The transport of Icelandic volcanic ash: Insights from northern European cryptotephra records. *Journal of Geophysical Research: Solid Earth*, *121*, 7177–7192. https://doi.org/10.1002/2016JB013350

Wen, S., & Rose, W. I. (1994). Retrieval of sizes and total masses of particles in volcanic clouds using AVHRR bands 4 and 5. *Journal of Geophysical Research*, *99*(D3), 5421–5431. https://doi.org/10.1029/93JD03340

Western, L. M., Watson, M. I., & Francis, P. N. (2015). Uncertainty in two-channel infrared remote sensing retrievals of a well-characterised volcanic ash cloud. *Bulletin of Volcanology*, *77*(8), 67. https://doi.org/10.1007/s00445-015-0950-y